Open Research Online

Carbon monoxide and far-infrared observations of the S 155-Cepheus B region

Journal Item

For guidance on citations see FAQs.

Version: Version of Record

Link(s) to article on publisher's website:
http://adsabs.harvard.edu/abs/1992A%26A...265..733M

oro.open.ac.uk

Carbon monoxide and far-infrared observations of the S 155–Cepheus B region

Nigel R. Minchin [1], Derek Ward-Thompson [2] and Glenn J. White [1]

[1] Department of Physics, Queen Mary and Westfield College, University of London, Mile End Road, London E1 3NS, U.K.
[2] Mullard Radio Astronomy Observatory, Cavendish Laboratory, Madingley Road, Cambridge CB3 0HE, U.K.

Abstract. We present maps of the CO J = 3→2 and ^{13}CO J = 2→1 molecular line and mid- to far-infrared continuum emission of the interface between the Cepheus B molecular cloud and the S155 HII region. Far-infrared dust colour temperature and optical depth maps show the molecular cloud to be externally heated and that the edge of the cloud is compressed by the expansion of S155. The data are compared with current models, and various dust grain parameters are derived. A *hotspot* is observed in the CO J = 3→2 emission line, at a position coincident with the radio continuum and infrared emission peaks. The infrared, radio continuum and molecular line emission from the hotspot are all consistent with it being a compact HII region, ionized by an embedded B1-B0.5 star. The position of the compact HII region, adjacent to the northwestern edge of Cep B, suggests it is the product of a phase of sequential OB star formation, which has already been responsible for the youngest subgroup of the Cepheus OB3 association. The mass of the cloud is estimated to be ∼100-200M$_\odot$.

Key words: stars: formation – stars: early-type – HII regions

1. Introduction

To the south of the Cepheus OB3 association of early-type stars lies the giant Cepheus molecular cloud, at a distance of about 725-800pc (Garrison 1970; Garmany 1973). This region was first mapped in the J = 1→0 transition of CO and ^{13}CO by Sargent (1977, 1979), revealing extended emission (20×60pc) with several hot cores, including Cep A, the hottest of which is Cep B. However, whereas Cep A has a bipolar outflow, H-H objects etc. (see Hartigan et al. 1986, and references therein), Cep B has none of these features, and appears to be a less evolved system.

Cep B lies near the northwestern edge of the cloud, adjacent to the HII region S155 (Sharpless 1959). The Cepheus OB3 association of O and B stars to the immediate north of Cep B are responsible for ionizing the S155 region. Felli et al. (1978) showed radio continuum observations of the region which show a ridge of emission, coincident with the interface between Cep B and the S155 HII region. There is also a radio plateau behind the ridge, towards the centre of Cep B. They present a compelling model in which the O7 star HD 217086, located behind the

molecular cloud, is the main source of ionizing radiation for S155 (see their Fig. 3 for a sketch of the region).

The far-infrared observations of Evans et al. (1981) also imply the strongest emission is from the interface between Cep B and S155, with dust temperatures decreasing away from the HII region, into the molecular cloud. These observations were interpreted as evidence that the heating source for the dust grains must be external to Cep B (but see Sect. 4.2). They also suggest that the high gas temperatures observed from the region may be due to collisional heating by the dust grains if the gas density is suitably high (n(H$_2$) > 4×10^4 cm^{-3}). Observations of the 6-cm H$_2$CO absorption line indicate that, although the average density of this region is much lower (n(H$_2$) = 1.1 - 1.4×10^3 cm^{-3}), high density condensations with n(H$_2$) > 4×10^4 cm^{-3} do exist (Panagia and Thum 1981).

In this paper we present observations of the CO J = 3→2 and ^{13}CO J = 2→1 emission from the CepB-S155 interface region. These observations were made at higher resolution than the Sargent (1977) observations of the CO J = 1→0 emission (29 and 15 arcsec respectively for the ^{13}CO J = 2→1 and CO J = 3→2 observations compared to Sargent's 65 arcsec) in an effort to reveal the detailed structure of the line emission from this region. *IRAS* observations of the mid- to far-infrared emission are presented to map the spatial distribution and temperature variations of the warm dust.

2. Observations

Observations of the ^{13}CO J = 2→1 transition were carried out using the National Radio Astronomy Observatory[1] (NRAO) 12-m telescope, located at Kitt Peak, Arizona, during January 1990. An eight-beam array receiver was employed, with each beam separated by 87 arcsec (3 FWHM antenna beamwidths). The telescope was rastered in such a way as to fill in the spacings between the beams at single beamwidth intervals, ensuring a fully-sampled map. Initially, a total of 500 spectra were observed, giving a total sky coverage of 800×600 arcsec. A further 314 spectra were then obtained within the central 400×450 arcsec of the map, with positions offset from the first grid so as to achieve an effective grid spacing of 15×15 arcsec for the central region.

Send offprint requests to: Nigel R. Minchin

A hybrid-spectrometer was used as the back-end, providing a total of 1536 channels, divided equally between the beams. The effective channel width of $\sim$195 KHz corresponded to a velocity resolution of $\sim$0.26 kms^{-1} at 220 GHz. The system noise temperature, including the sky, was $\sim$2000K, the telescope beamwidth was 28 arcsec and the on-source integration times were 30 seconds per point.

Observations of the CO J = 3$\rightarrow$2 transition (346 GHz) were made using the James Clark Maxwell Telescope[2] (JCMT), located on Mauna Kea, Hawaii, during April 1991. A dual-polarisation Schottky mixer system (receiver B2) was used, with an acousto-optical spectrometer backend. A total of 338 positions were observed on a grid with 20 arcsec spacing, giving a total sky coverage of 450$\times$300 arcsec. The on-source integration times were 60 seconds per position, the system noise temperature was $\sim$2400K and the telescope beamwidth was 15 arcsec.

The molecular line data presented in this paper are all calibrated into units of T$_R^*$ (Kutner and Ulich 1981), and as such have been corrected for all atmospheric, ohmic and spillover losses. The values of η_{fss} used were 0.7 for the NRAO 12-m data and 0.75 for the JCMT data.

IRAS Calibrated Reconstructed Detector Data (CRDD) – 2nd calibration – were extracted from archive tapes for a 2$\times$2-degree square region centred on Cep B, and reduced using standard STARLINK *IRAS* and EDRS/EDRSX routines. Particular attention was paid to de-striping the data by carefully removing background offsets from each scan individually, using an iterative process, in the manner described by Ward-Thompson et al. (1989). A 2-degree field was required to determine the background level to sufficient accuracy, and a constant offset was applied to each scan. The region was found to be moderately free of confusion by Zodiacal and Galactic Plane emission, and no further de-striping was necessary. The data at all four wavebands (centred at 12, 25, 60 and 100 μm) were mapped into images with a pixel size of 1 arcminute. See IRAS *Explanatory Supplement* (1988) for further details.

3. Results

3.1. CO observations

Maps of the CO J = 3$\rightarrow$2 integrated intensity between -13 and -12 kms^{-1} from the Cep B region are shown in Fig. 1. A greyscale image, with isophotal contours overlayed, is shown in Fig. 1a and an isophotal contour map, with the four highest contours of the CO J = 1$\rightarrow$0 emission (taken from Fig. 8a of Sargent (1977)) overlaid, is shown in Fig. 1b. The most striking feature on both the maps is the strong peak or *hotspot* at the northwestern edge (-160,+140), close to the O7 star HD217086 (the probable ionizing source for the HII region S155), where the highest values of T$_R^*$ (up to 48K) were detected. These figures clearly show the steep drop-off in emission at the molecular cloud edge. The position of the hotspot is clearly offset from Sargent's J = 1$\rightarrow$0 emission peak (between 100 and 200 arcsec), but is roughly coincident with the far-infrared peak found by Evans et al. (1981) and radio continuum source number 9 in the 610 MHz map of Felli et al. (1978), and is located at R.A. (1950) = 22^h 55^m 08^s, Dec. (1950) = 62^o 21$'$ 30$''$.

Figure 2 a-f shows the individual velocity channel maps of the CO J = 3$\rightarrow$2 emission from -10 to -16 kms^{-1} at intervals of 1 kms^{-1}. The hotspot lies at the apex of a triangular shaped *ridge* of intense emission, which is most clearly seen in Figs. 2d and 2e at velocities of -11 to -13 kms^{-1}. This feature is consistent, both in its general morphology, and also its velocity, with the data of Sargent (1977), who found that the bulk of the J = 1$\rightarrow$0 emission forms a wedge shape whose apex points to the NW, and lies at a velocity of -12 kms^{-1}. The ridge forms a well-defined boundary edge to the north and west of the molecular cloud and thus delineates the molecular cloud/photo-dissociation region (PDR) interface.

It can also be seen that there is a great deal of emission from the hotspot at velocities of -13 to -15 kms^{-1}. This is slightly blue-shifted relative to the bulk of the molecular cloud (Sargent 1977), but it is noted that the V$_{LSR}$ of S155 is $\sim$-15 kms^{-1} (Miller 1968). We therefore suggest that the CO hotspot may be physically associated with the HII region S155, and its ionizing star, which are located behind the molecular cloud, and that the expansion of the HII region and the associated shocks could have accelerated gas at the apex of the triangular ridge, along the line of sight towards us. Furthermore, the edge of the cloud is much less clearly defined at velocities -13 to -15 kms^{-1} (ie: different to the V$_{LSR}$ of the cloud) indicating disruption of the cloud edge. The hotspot is elongated, and for velocities between -13 and -12 kms^{-1} is resolved into two peaks aligned NW-SE. At more blue-shifted velocities (-15 to -14 kms^{-1}) emission from the hotspot is elongated roughly perpendicular to this in the NE-SW direction, possibly indicating some form of expansion of the hotspot.

Also evident in Fig. 2 is a fan-shaped feature lying about 200 arcsec to the south of the hotspot, which is resolved into two distinct components, aligned along an approximate E-W direction. The western component is compact and roughly circular, whilst the eastern component is extended and narrows towards the west. The bulk of the emission from this feature is observed between velocities -12 and -10 kms^{-1}, slightly red-shifted relative to the bulk of the CO J = 1$\rightarrow$0 emission. The implication is that this fan feature is physically distinct from the molecular cloud/S155 interface (which is located on the far side of the cloud), but is clearly associated with the molecular cloud, possibly on the near face. The position of the fan (adjacent to the ionization front to the west of Cep B) and its morphology in the east-west direction (widening into the cloud), imply that a star to the west of Cep B is responsible for the heating of this region. The only star suitably close and in the right direction is the B1 star HD217061.

Figure 3 is a greyscale image, with isophotal contours overlayed, of the ^{13}CO J = 2$\rightarrow$1 total integrated intensity from the same region as Figs. 1 and 2. Figure 4 shows the individual velocity channel maps of the ^{13}CO J = 2$\rightarrow$1 transition from -10 to -14 kms^{-1} at intervals of 1 kms^{-1}. Similar to Figs. 1 and 2, the ^{13}CO emission is most intense along a ridge feature at the molecular cloud/PDR interface, though the drop-off in intensity is less marked. The ^{13}CO emission is produced over a somewhat narrower velocity range (-14 to -10 kms^{-1}) than the CO emission (-16 to -10 kms^{-1}). However the most striking difference between the CO and ^{13}CO maps is the relative lack of ^{13}CO emission from the position of the CO hotspot (marked by a cross). The implications of this are discussed in Sect. 4.2.
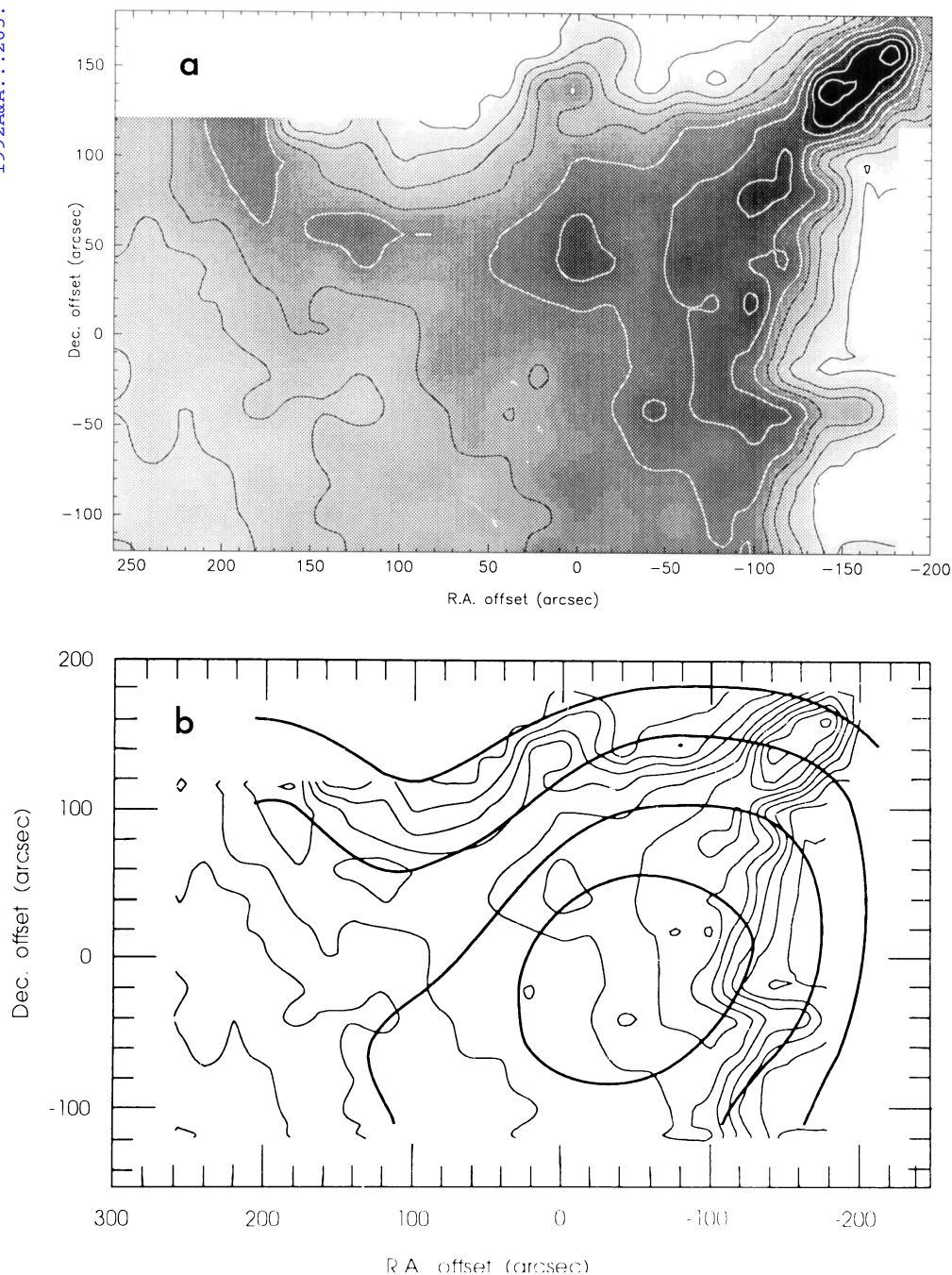
Fig. 1(a) Greyscale image, with isophotal contours overlayed, of the CO J = 3→2 integrated intensity between -13 and -12 kms^{-1} from the Cep B/S155 interface region. The base level contour is at 5 K-kms^{-1} and the contour interval is 12 K-kms^{-1}. The (0,0) position is at R.A. (1950) = $22^h55^m30^s$ and Dec. (1950) = $+62°19'00''$. (b) Isophotal contour map of the CO J = 3→2 integrated intensity between -13 and -12 kms^{-1} from the same region as (a) with the highest four contours of the CO J = 1→0 emission overlayed as bold lines (taken from Fig. 8a of Sargent (1977)

3.2. IRAS observations

Figure 5 a-d shows the *IRAS* 12, 25, 60 and 100 μm intensity maps respectively. The far-IR emission shows basically the same morphology at all four wavelengths. The emission peaks near the edge of the molecular cloud/HII region interface, at a position roughly coincident (to within *IRAS* pointing errors) with the CO hotspot (discussed in Sect. 3.1), the far-infrared peak of Evans et al. (1981), and radio continuum peak 9 of Felli et al. (1978). There is a tail of low-level emission, extending from the peak towards the southeast, i.e. towards the centre of the molecular cloud. The overall morphology at all four wavebands is somewhat similar to the 125-μm map of Evans et al. (1981).

The IRAS *Point Source Catalogue* fluxes are often inaccurate in confused regions, or when dealing with extended sources, both of which conditions are true in the case of Cep B. So we measured the fluxes in a 6×6 arcminute square aperture, centred on the position quoted earlier of the CO hotspot, at all four wavebands shown in Fig. 5. This aperture was chosen to pick up only the flux associated with the IR peak, and not the extended emission, and because it most closely mimics the area in which Evans et al. measured the 125-μm flux. These fluxes are listed in Table 1, along with the fluxes of Evans et al., who claim that their 55-μm flux is a lower limit due to undersampling. Also listed are the AFGL fluxes of Price and Walker (1976). The errors in the *IRAS* fluxes are estimated to be $\sim \pm30$%. The quoted fluxes do not contain any colour corrections, as the corrections at the
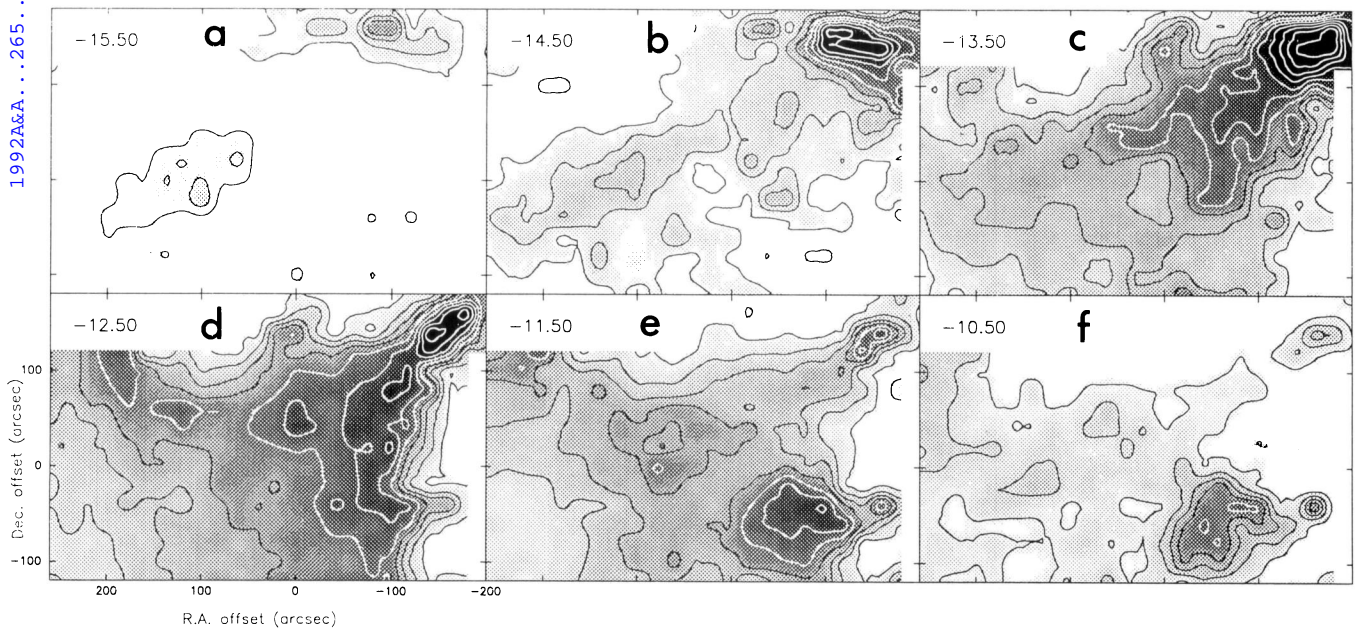
736

Fig. 2. Channel maps of the CO J = 3→2 integrated intensity from the Cep B/S155 interface region. Each map is a greyscale image with isophotal contours overlayed. The base level contour is at 2 K-kms^{-1} and the contour interval is 4 K-kms^{-1}. The channel width is 1 kms^{-1}, and the central velocity for each channel is labelled. The (0,0) position is the same as for Fig. 1.
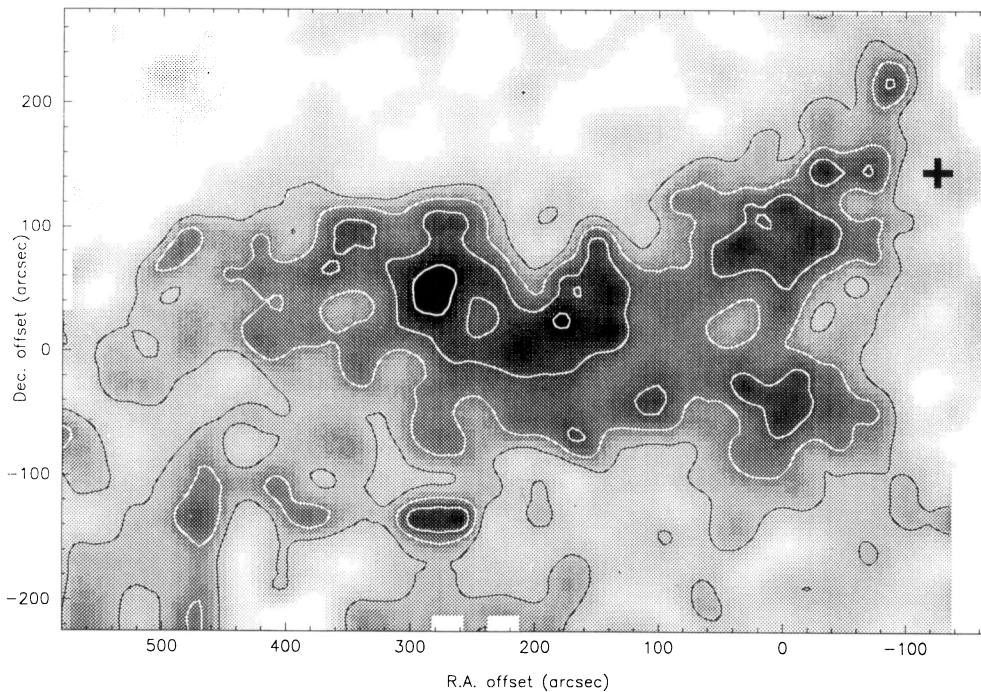

Fig. 3. Greyscale image, with isophotal contours overlayed, of the ^{13}CO J = 2→1 total integrated intensity from the Cep B/S155 interface region. The base level contour is at 10 K-kms^{-1} and the contour interval is 5 K-kms^{-1}. The (0,0) position is at R.A. (1950) = 22^{h}55^{m}26^s and Dec. (1950) = +62°19'00''. The position of the CO J = 3→2 hotspot peak is marked by a cross

temperatures derived below are considerably less than the errors (see IRAS *Explanatory Supplement* 1988).

These fluxes can also be compared to the *IRAS* fluxes quoted by Gordon (1990), who used a somewhat larger, circular aperture, which may have included flux from the more extended emission. Our fluxes only agree at the limits of the combined errors, and our fluxes lie below Gordon's, although ours agree better with the earlier work. This is probably the result of the aperture effect just mentioned, or may be a result of our careful background subtraction, but it leads to differences in our derived properties.

Specifically, we obtain a lower mean dust temperature for the cloud (see below), however our different values are justified in Sect. 4.3.

The dust colour temperature (T_D) and 100-μm optical depth (τ_{100}) can be calculated from the ratio of the 60- to 100-μm flux densities using the equation (Gordon 1987):

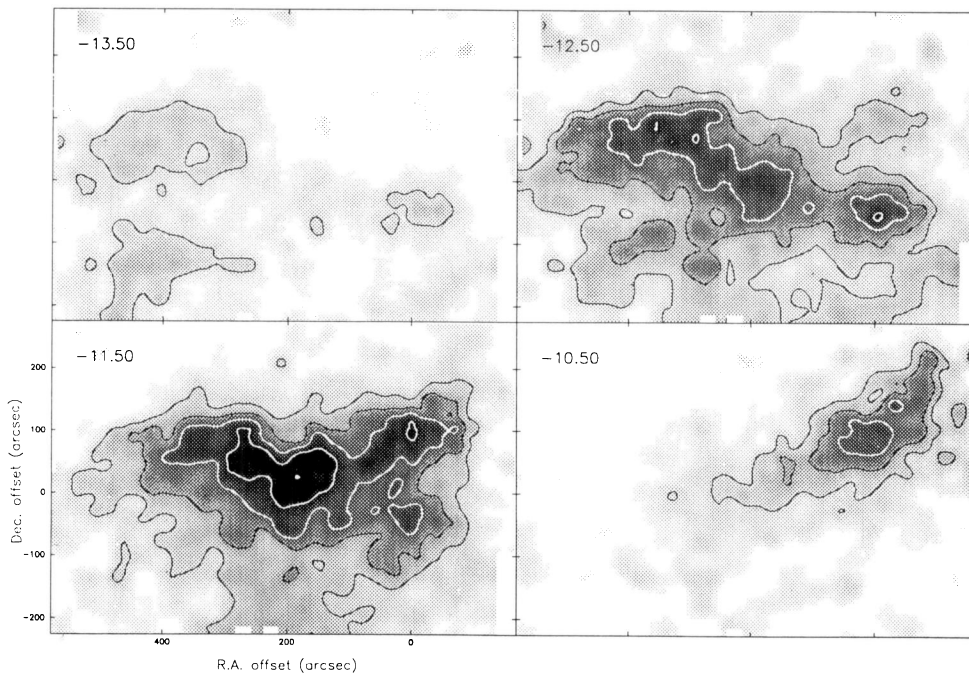$$F_v = \Omega B(v, T)(1 - e^{-\tau}), \tag{1}$$

and hence:

Fig. 4. Channel maps of the ^{13}CO $J = 2\rightarrow1$ integrated intensity from the Cep B/S155 interface region. Each map is a greyscale representation with isophotal contours overlayed. The base level contour is at 3 K-kms^{-1} and the contour interval is 2 K-kms^{-1}. The channel width is 1 kms^{-1}, and the central velocity is labelled. The (0,0) position is at R.A. (1950) = $22^h55^m26^s$ and Dec. (1950) = $+62°19'00''$

Table 1. *IRAS* flux densities in Jy for a 6×6 arcminute square aperture of Cep B, together with data taken from the literature. ^{a}Indicates data taken from Price and Walker (1976). ^{b}Indicates data taken from Evans et al. (1981). No colour corrections have been used for the *IRAS* data. 3-σ errors in the *IRAS* data are estimated to be $\sim \pm30\%$. See text for discussion.

λ/μm	Flux/Jy
4.3	48^a
11	110^a
12	133
19.8	245^a
25	472
55	>2150^b
60	3945
100	5927
125	6300^b

$$\frac{F_{v_1}}{F_{v_2}} = \frac{B(v_1, T)}{B(v_2, T)} \cdot \frac{(1 - e^{-\tau_1})}{(1 - e^{-\tau_2})}. \qquad (2)$$

where B(v,T) is the black-body function, Ω is the source apparent solid angle (which cancels) and τ is the optical depth. The method first assumed that the cloud was optically thin at these wavelengths ($\tau \ll 1$) and thus of similar optical depth at 60 and 100-μm, hence the second term on the right hand side of equation 2 could be ignored while calculating T at each pixel. Then, using the calculated temperature, the optical depth at each wavelength was calculated at every pixel using:

$$\tau = (v/v_c)^{\beta}, \qquad (3)$$

where v_c is the critical frequency at which the optical depth is unity, and β is the dust emissivity spectral index, which was taken to be equal to 1. The process then iterates to a convergent

solution. The results are displayed in Fig. 6, where contours of 100-μm optical depth (thick lines) are shown overlaid upon the colour temperature contours (thin lines). The position of peak far-IR emission (R.A. = 22^h 55^m 08^s, Dec. = $62°$ $21'$ $30''$) is marked with a cross and the position of HD 217086 is marked with an asterisk.

It can be seen from Fig. 6 that the dust grains responsible for the 60 and 100-μm emission have temperatures in the range 31-47K. This compares well with the peak gas temperature of 48K found in Sect. 3.1, and shows that for the bulk of the cloud core, the gas and the dust grains responsible for the far-IR emission are probably in thermal equilibrium. The optical depths lie in the range 4×10^{-3} to 2.3×10^{-2} (justifying the initial optically thin assumption). The peak of the optical depth lies in the core of the molecular cloud, as would be expected, to the southeast of the CO hotspot. However the dust temperature peak lies close to the CO hotspot, and the higher temperature contours (~45K) lie in a ridge along the northwestern side of the optical depth peak. This shows that the dust is not being heated from the centre of the molecular cloud core, but rather from the direction of the S155 HII region and the CO hotspot. Also lying to the northwest is the O7 star HD217086 associated with the HII region, and we suggest that the dust at the molecular cloud/HII region interface is being heated by the Lyman continuum photon flux from HD217086 and thus has the highest values of T$_D$. As the expansion of the ionization shock front compresses the molecular cloud edge, the dust optical depth immediately behind the molecular cloud/HII region interface is enhanced relative to the rest of Cep B. A similar morphology is observed in the molecular cloud M17 (Gatley et al. 1979; Hobson 1992).

To determine the mean properties of the whole Cep B far-IR peak, the fluxes measured above in a 6×6 arcminute square aperture were used. Figure 7 shows the fluxes from Table 1 plotted against frequency on a logarithmic scale. Also shown on Fig. 7 is a grey-body curve, consistent with the data, of the form shown in equation 1, for the 60 to 100-μm data, and the Evans *et al.* data. The parameters of the grey-body are T = 39K, β = 1,
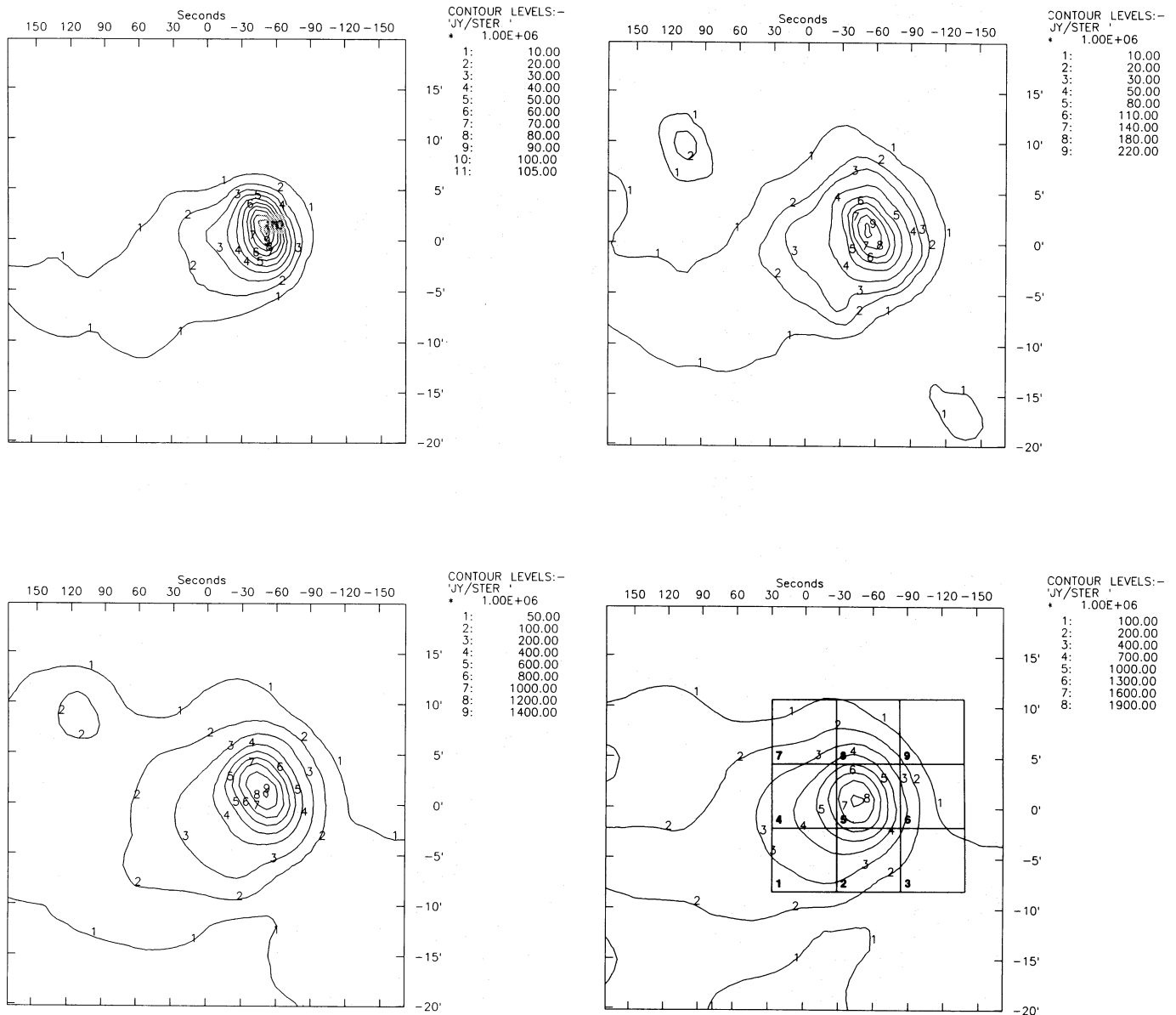
738

Fig. 5. Isophotal contour maps of the Cep B/S155 interface region at all four IRAS bands, centred at (a) 12, (b) 25, (c) 60 and (d) 100 μm. The (0,0) position is at R.A. (1950) = $22^h 56^m 00^s$ and Dec. (1950) = $+62°20'00''$. The numbered boxes in (d) show the areas in which the flux ratios were taken for Fig. 8

$\Omega = 2 \times 10^{-7}$ steradians and $v_c = 10^{14}$ Hz. Clearly this is not a unique fit, due to the small number of data points, and the larger number of free parameters. However, the curve is consistent with the mean of the parameters for Cep B seen in Fig. 6, and the temperature of 39K appears to be representative of the bulk of the cloud core. The excess near-IR emission above the curve, seen by both *IRAS* and previous authors, shows that more than one dust grain population is present (see Sect. 4.1). The total luminosity under the data points of Fig. 7 from 4 to 125 μm was measured and found to be ~14,000$L_\odot$ for a source distance of 725pc.

The total fluxes for the CepB far-IR peak can also be used to derive the nature of the object, by comparing its *IRAS* colours with statistical studies of *IRAS* sources carried out by other authors. For example, using the system of Walker and Cohen (1988) who use the magnitude scale, as defined by the IRAS *Explanatory Supplement* (1988), we find Cep B has colours: [12] - [25] = 2.9, [25] - [60] = 4.2 and [60] - [100] = 1.6. Thus it occupies a region on a [60] - [100] versus [25] - [60] colour-colour diagram consistent with it being an HII region, and in [25] - [60] versus [12] - [25] space it lies on the edge of the areas occupied by HII regions and reflection nebulae (Walker et al. 1989). Crawford and Rowan-Robinson (1986) simply took the logarithm of the flux ratio of a sample of compact HII regions and examined where they lay in colour-colour space. For Cep B these ratios are [100-60] = 0.17, [60-25] = 0.92 and [25-12] = 0.55, which is consistent with an HII region of moderate surface brightness. This will be discussed further in Sect. 4.2.
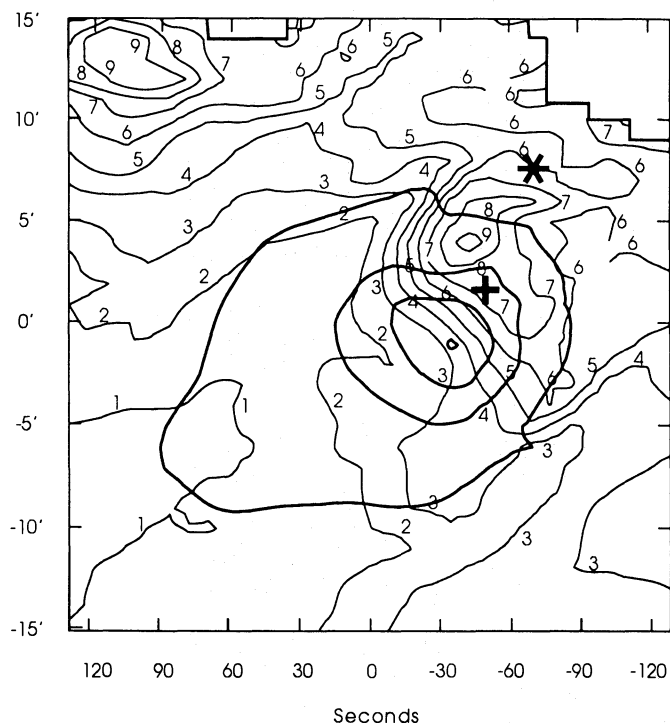
Fig. 6. Isophotal contour map of the 100-μm optical depth (thick lines) overlaid on the dust colour temperature (thin contours), calculated from the 60 and 100 μm flux densities. The optical depth contours are at 0.004, 0.01, 0.015 and 0.023; the dust colour temperature base level contour is at 31K and the contour interval is 2K. The (0,0) position is the same as for Fig. 5. The position of peak far-IR emission, R.A. (1950) = $22^{h}55^{m}08^{s}$ and Dec. (1950) = $+62^{o}21'30''$, is marked with a cross and the position of the O7 star HD 217086 is marked with an asterisk

Fig. 7. *IRAS* flux densities of the Cep B far-IR peak measured in a 6×6 arcminute square aperture, compared with the fluxes of Evans *et al.*, and Price & Walker. The horizontal bars on *IRAS* data simply show the detector bandwidths. A 39K grey-body consistent with the data is shown. See text for discussion

4. Discussion

4.1. Far-IR colour temperatures and dust grain parameters - comparison with the DBP model

Spatial variations in the different far-IR colour-colour ratios can be used to determine dust grain parameters. The recent model for dust grain size distributions of Désert, Boulanger and Puget (1990 – hereafter DBP) has many inherent attractions, not least of which is that it is based empirically upon both the *IRAS* data of many environments within our Galaxy from dense clouds to the diffuse ISM, and also the well-known form of the interstellar extinction curve. It thus aims to find the simplest grain size distribution which explains both the absorption and emission observations of the interstellar medium, to predict the basic grain optical properties, and to define the astrophysical implications in different environments. We therefore decided to compare our *IRAS* data of the Cep B region with the DBP model.

The DBP model is more sophisticated than the classic MRN model (Mathis, Rumpl and Nordsieck 1977) in that it contains three dust grain components (the smallest number consistent with all the available astrophysical and laboratory data):- (i) polycyclic aromatic hydrocarbons (PAH's), (ii) very small grains (VSG's) and (iii) big grains (BG's). The PAH's are used to explain the far-UV extinction curve and the near-IR emission. The VSG's explain the 220nm bump in the extinction curve and the mid-IR emission, and may be composed chiefly of graphite. The BG's account for the visible extinction and the far-IR and sub-
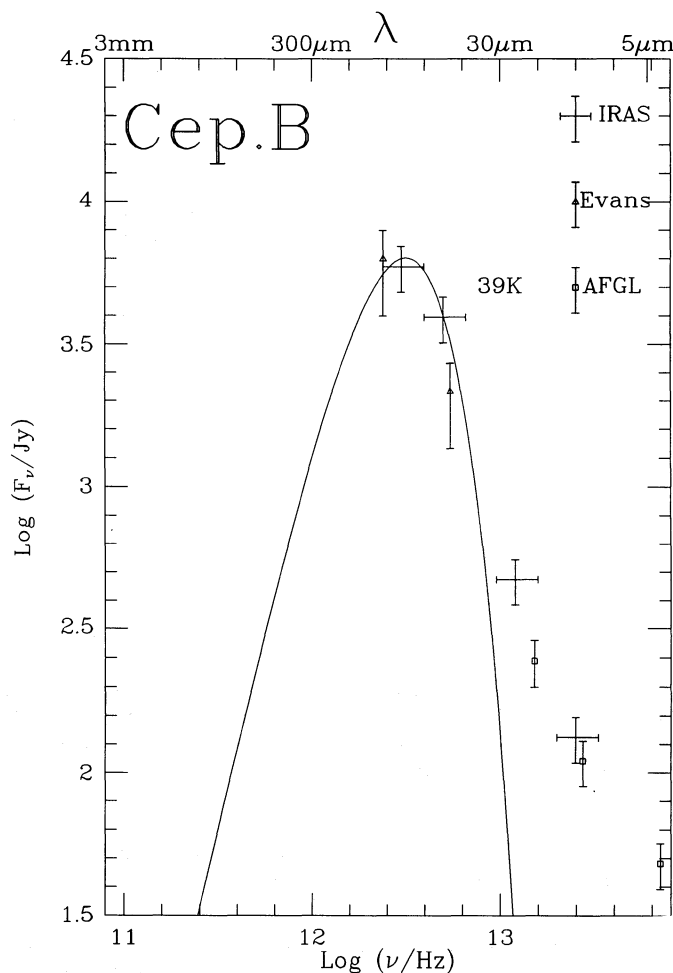
millimetre continuum emission, and are probably silicates which may have grain mantles. All three components have a power-law size distribution.

In the following, we leave the majority of the parameters at the optimum values ascertained by other means, and merely explore the effects of varying the interstellar radiation field (ISRF) to which the grains are exposed, and also the lower limit cut-off of the VSG size distribution, after the manner of Désert (1986) and Greene and Young (1989 – hereafter GY). Using the predicted IR emission curve of the model (such as that shown in Fig. 4 of DBP) it is possible to generate a series of curves in IR colour-colour space (such as are shown in Désert Fig. 2 and GY Fig. 4) showing the dependence of IR colours on these two parameters.

Figure 8 shows a plot of the 12 to 25-μm flux density ratio against the 60 to 100-μm flux density ratio. The solid line has a VSG radius lower limit cutoff of 1.5nm, which is equal to the maximum size of the PAH's, and hence represents a continuous grain size distribution from PAH's to BG's. The dashed line has a cutoff of 10nm, and hence represents a more bimodal distribution. X is defined as the ratio of the value of the ISRF to that in the solar neighbourhood, and three values of X are marked on each
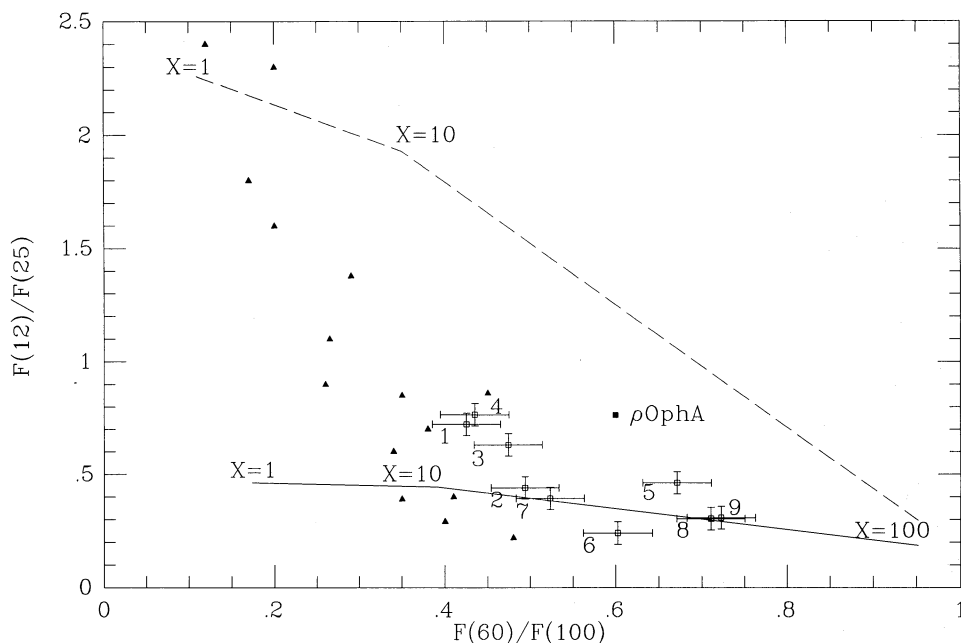
Fig. 8. Infra-red colour-colour plot of our data compared to the DBP model. The solid line represents a lower limit grain size cut-off for the VSG's of 1.5nm, and the dashed line represents a cut-off of 10nm, for varying strengths of the interstellar radiation field, X. The triangles are data taken from Désert (1986), and the solid square is for the ρ Oph A core (position 5 of GY). Our data are numbered according to the areas shown on Fig. 5, and have 1-σ error-bars representative of the mean spread of the measurements in 1-arcminute square pixels. See text for discussion

curve. The solid triangles are the data of Désert (1986) for 15 Galactic molecular clouds and the solid square is the data for the ρ Oph A core of GY (their position 5).

Our data were binned into 7×7 arcminute square apertures, and the colour ratios measured within each square. This corresponds to ~1.4×1.4pc at the distance of Cep B. This is the same physical size as the bins used by GY for ρOph, who also compared their data to those of Désert. Our data are plotted on Fig. 8 with 1-σ error-bars calculated from the typical mean scatter in the values measured within the 1-arcminute pixels making up each bin. The points are numbered to illustrate which part of the Cep B cloud they represent, as shown in Fig. 5.

The four points which lie closest to the S155 HII region (numbers 5, 6, 8 and 9) all lie below and to the right of the other points in Fig. 8, with a predicted ISRF of ~30-50 times the solar neighbourhood value. The remaining five points (numbers 1, 2, 3, 4 and 7), which are further from S155, lie more to the left on Fig. 8, with a predicted ISRF of only ~10-20 times the local value. This further confirms that the chief heating source of Cep B lies to the northwest, in the vicinity of S155.

Six of our data points lie on or close to the solid curve of Fig. 8, indicating that in these regions there is no lower cut-off in the VSG grain size distribution, and there is a continuous distribution of sizes from PAH's to BG's. Three of the points (numbers 1, 3 and 4) lie significantly above the solid line, tending to indicate that for these regions there may be a cut-off in size. These points are also the ones with the lowest ISRF, and mirror the trend observed in Désert's data that the points furthest to the left also show a tendency to spread above the solid line, and tend towards the dashed line, where there are no VSG's. This seems to be saying that in regions of high ISRF there are more small dust grains, perhaps indicating that here large grains are broken up into smaller grains, possibly by shocks, which are

known to exist in such regions. The exact mechanism of this process is unclear, although it may involve the removal of the carbon mantles (discussed by DBP) from silicate grains.

The one exceptional data point on Fig. 8 appears to be ρOph A, which lies above and to the right of the other data, indicating a paucity of small grains. However, it is also well documented that the ratio of total to selective extinction ($R = A_V/E_{B-V}$), which is an indicator of grain size, is higher for ρOph than other clouds, or the general ISM (eg: Whittet, van Breda and Glass 1976). This is therefore consistent with its position on Fig. 8.

4.2. The CO hotspot - a compact HII region?

The ionization and energy balance of S155 was discussed by Felli et al. (1978). By considering the radio continuum emission at 0.610 and 4.995 GHz from the molecular cloud/S155 interface, they concluded that the O7 star HD217086 (a member of the Cepheus OB3 association) was externally illuminating the edge of Cep B and producing the HII region. The fact that HD217086 is the main source of ionization for S155 is not in doubt, and we have already shown that the hottest dust lies in the region of the CO hotspot, towards S155. However we now consider whether HD217086 could provide enough stellar Lyman continuum photon flux (N_L^*) to explain the 4.995 GHz continuum emission (N_L^R) from the position of the far-IR peak/CO hotspot (source 9 of Felli et al. 1978).

At 4.995 GHz Felli et al. (1978) observed a continuum flux of 0.15 ±0.02 Jy from source 9. Using the formula given by Mezger and Henderson (1967), they equate this to a total supply of stellar Lyman continuum flux (N_L^*) = $8.5 \times 10^{45} s^{-1}$. We repeated this calculation using equation (1) from Bally et al. (1983) and derived a value of (N_L^*) = $1 \times 10^{46} s^{-1}$, in reasonable agreement with Felli

et al. From Panagia (1973) HD217086, an O7 ZAMS star, emits a flux of Lyman continuum photons $(N_L^*) = 4.2 \times 10^{48} s^{-1}$.

Assuming the projected distance between HD217086 and source 9 to be the true separation, then they are 5 arcminutes apart, corresponding to ~1.2pc at a distance of 725pc. At 4.995 GHz Felli et al. (1978) observed source 9 to be an extended feature with an angular size of ~0.1pc. Therefore the Lyman continuum flux from HD217086 incident upon source 9 is $\sim 2 \times 10^{45} s^{-1}$, although this does not take into account flux dilution between HD217086 and source 9, or an ionization efficiency factor, so it is an upper limit.

Clearly, as even this upper limit is a factor of 5 too low to account for the radio continuum emission from source 9, HD217086 cannot be the sole source of ionization for this feature. As the only other members of the Cepheus OB3 association are either of distinctly lower luminosity or considerably further away, this implies that the CO hotspot (source 9) must be a compact HII region, ionized by an embedded star. This confirms the evidence of its *IRAS* colours discussed in Sect. 3.2. We designate this object CepB-C1.

We can estimate the spectral type of the embedded star using the derived value of N_L^* $(1 \times 10^{46} s^{-1})$ and the infrared emission for CepB-C1. This can only be approximate, as it is not possible to separate the heating effects of CepB-C1 and HD217086. From Panagia (1973) this number of stellar Lyman continuum photons will be produced by a B1-B0.5 star. The infrared fluxes for CepB-C1, taken from Table 1 and Fig. 7, were shown earlier to give an IR luminosity of $\sim 14,000 L_\odot$. Assuming that the IR luminosity contributes ~50% of the total luminosity from CepB-C1, we can make a rough estimate of the spectral type of the embedded star. From Table 1 of Panagia (1973) an embedded star responsible for the far-IR emission from CepB-C1 would need to be of spectral type B1-B0.5. Thus both the radio continuum and infrared emission are consistent in implying the ionizing star for CepB-C1 is of spectral type B1-B0.5.

As noted in Sect. 3.1, there is a distinct lack of ^{13}CO emission from the position of the CO hotspot, compared to the ridge of emission at the CepB/S155 interface region. The ratio of $T_R^*(CO\ 3\rightarrow 2)/T_R^*(^{13}CO\ 2\rightarrow 1)$ is generally between 2 and 3 along the ridge [where typically $T_R^*(CO\ 3\rightarrow 2) = 25\ \pm 5K$ and $T_R^*(^{13}CO\ 2\rightarrow 1) = 13\ \pm 3K$], but for the hotspot $T_R^*(CO\ 3\rightarrow 2)/T_R^*(^{13}CO\ 2\rightarrow 1) \sim 10$ $[T_R^*(CO\ 3\rightarrow 2) = 48\ \pm 2K$ and $T_R^*(^{13}CO\ 2\rightarrow 1) = 5\ \pm 2K]$. The antenna temperatures observed from the ridge and hotspot were analysed using a Large Velocity Gradient (LVG) model. Assuming that $T_{kin} = 60K$ for the hotspot, $n(H_2) = 1\ \pm 0.2 \times 10^5$ cm^{-3}, $\tau(^{13}CO\ 2\rightarrow 1) = 0.2\ \pm 0.1$, and $\tau(CO\ 3\rightarrow 2) = 10\ \pm 5$. Whilst for the molecular cloud/S155 interface region, assuming $T_{kin} = 40K$, then $n(H_2) = 1\ \pm 0.2 \times 10^3\ cm^{-3}$, $\tau(^{13}CO\ 2\rightarrow 1) = 4\ \pm 2$, and $\tau(CO\ 3\rightarrow 2) = 60\ \pm 20$.

Clearly the ^{13}CO and CO optical depths along the line-of-sight to the hotspot are distinctly lower than along the line-of-sight to the rest of the molecular cloud/S155 interface region. This conclusion, in conjunction with the relatively high values of $n(H_2)$ and T_{kin}, are consistent with the presence of an embedded compact HII region at the position of the CO hotspot. A thin dense layer of gas in the region adjacent to the molecular cloud/compact HII region interface will be heated to a relatively high kinetic temperature by the dust, which is itself heated by the Lyman continuum flux from the embedded B1-B0.5 star. As CepB-C1 is positioned at the edge of Cep B, the optical depth along the line-of-sight is relatively low, allowing us to observe emission from the hotspot.

The position of CepB-C1, adjacent to the molecular cloud/S155 interface, suggests it is the product of sequential star formation due to shock compression of the molecular cloud. Elmegreen and Lada (1977) have proposed a model in which star formation proceeds through a molecular cloud (from the edge inwards) in a sequential manner, producing distinct subgroups of OB stars. This already appears to be happening with the Cepheus OB3 association, with star formation moving in the northeast-southwest direction (Blaauw 1964; Sargent 1979). There are two subgroups to the Cepheus OB3 association, with the youngest close to Cep A and Cep B (the illuminator of S155, HD217086, is a member of this group). The presence of a compact HII region adjacent to a molecular cloud/HII interface is not unique, with M17-UC1 being a well known example (Felli, Johnston and Churchwell 1980; Felli, Churchwell and Massi 1984; Hobson 1992).

4.3. The mass of dust and gas in Cep B

The mass of dust which is emitting in the far-IR (assuming the source is optically thin in this range) can be calculated (Hildebrand 1983) from the equation:

$$M_d = \frac{4a\rho D^2 F_v}{3B(v,T)Q_v}, \qquad (4)$$

where a is the mean grain radius, ρ is the density of dust grain material, D is the distance to the cloud and Q_v is the emissivity. Using the 100-μm flux density in Table 1, which we have found in Sect. 3.2 to be optically thin – $\tau \sim 0.02$ – we can calculate the mass of dust in the 6×6 arcminute square aperture. Using typical values for each of the parameters (after Hildebrand), the total mass of dust was found to be $0.66 M_\odot$. Typical values for the gas-to-dust mass ratio in dark clouds (Hildebrand 1983) are 100-200. Taking 150 leads to a cloud mass of $\sim 100\ \pm 35 M_\odot$.

The absolute errors in this mass estimate are difficult to assess (the error quoted above is simply due to the uncertainty in the gas-to-dust ratio), and could be a factor of two or more, due to the nature of the assumptions upon which it is based, and the fact that the fit to the data in Fig. 7 may not be unique. Gordon (1990) measured the *IRAS* flux densities in a slightly larger area, for comparison with Evans et al. (although we believe our boxes are more comparable), and obtained a value for T some 10K higher than our value, and a correspondingly higher value of τ. Hence, in his more optically thick case, he obtains a cloud mass of $6\ \pm 24 M_\odot$.

However, it is not clear exactly what region this corresponds to, as he shows neither *IRAS* nor submillimetre maps of the region, and merely quotes fluxes. Furthermore, his mass estimate relies upon a 1.3-mm flux density, which he quotes as only a marginal detection, with uncertainties of a factor of 5, and corrects the flux with a beam filling factor which he claims can introduce further uncertainties of a factor of 10. Clearly, within these error-bars, our values for the mass are consistent. However, we can check the cloud mass from our ^{13}CO data.

The mass of ^{13}CO in Cep B can be calculated (for example: Rohlfs 1986) from the integrated intensity map of $^{13}CO(J=2\rightarrow 1)$ in Fig. 3 using the equation:

$$N_{J+1} = \frac{3\epsilon_0 k}{2\pi^2 \mu_e^2 v_{10}} \cdot \frac{2J+3}{(J+1)^2} \int T_R(v)dv, \qquad (5)$$

where v_{10} is the *lowest* transition (~110 GHz), $T_R(v)$ is the observed Rayleigh-Jeans brightness temperature of the J+1 → J

transition as a function of velocity, and other symbols take their usual meanings.

Integrating the emission over all velocities in the same 6×6 arcminute square region of Fig. 3 as was used above for the dust, this gives the total number of emitting ^{13}CO molecules in the J = 2 state (assuming this is optically thin). Using a typical excitation temperature of 40K for the region, we calculate $\sim 1/4$ of the total number of molecules are in this state. Then taking the abundance of ^{13}CO relative to H_2 to be 10^{-6}, we obtain a total gas mass in this region of $\sim 200 M_\odot$.

The uncertainties in this estimate could also be as high as a factor of 2, given the nature of the inherent assumptions. Therefore we would say this is consistent with our mass estimate from the *IRAS* data, but inconsistent with Gordon's mass estimate. We feel this justifies our different values for the grey-body fit to the infrared data.

5. Conclusions

The interface region between the extended HII region S155 and the molecular cloud Cep B has been studied using high-resolution CO(J = 3→2) and ^{13}CO(J = 2→1) emission line observations, in conjunction with *IRAS* data. The dust colour temperatures and optical depths, derived from the far-infrared emission, imply that Cep B is partly heated externally by members of the Cepheus OB3 association.

Comparison with theory shows that the data are consistent with a grain size distribution which is continuous from PAH's to large silicate grains, and that the radiation field increases towards the O7 star HD217086. Furthermore, the CO observations imply that this star is one of the main sources of ionization, and is situated behind the molecular cloud, as suggested in a model by Felli *et al.* (1978). The edge of the molecular cloud is shock-compressed by the expanding ionization region. The B1 star, HD217061, is also responsible for heating part of the western edge of CepB. The mass of the cloud, as calculated from both the gas and dust emission, is ~ 100-$200 M_\odot$.

Both the infrared and molecular line observations imply there is a compact HII region, here designated CepB-C1, situated at the edge of the molecular cloud and adjacent to S155. The spectral type of the embedded star, as implied from the radio continuum (Felli et al. 1978) and far-IR emission, is B1-B0.5. We suggest that the star powering CepB-C1 has been produced by sequential OB star formation, already responsible for the youngest subgroup of the Cepheus OB3 association.

References

Bally J., Snell R. L., Predmore R., 1983, ApJ 272, 154
Blaauw A., 1964, ARA&A 2, 213
Crawford J., Rowan-Robinson M., 1986, MNRAS 221, 923
Désert F. X., 1986, In: Light on Dark Matter, ed. Israel F. P., Reidel, Dordrecht, p. 213
Désert F. X., Boulanger F., Puget J. L., 1990, A&A 237, 215 (DBP)
Elmegreen B. G., Lada C. J., 1977, ApJ 214, 725
Evans N. J., Becklin E. E., Beichman C., Gatley I., Hildebrand R. H., Keene J., Slovak M. H., Werner M. W., Whitcomb, S. E., 1981, ApJ 244, 115
Felli M., Tofani G., Harten R. H., Panagia, N., 1978, A&A 69, 199
Felli M., Johnston K. J., Churchwell E., 1980, ApJ 242, L157
Felli M., Churchwell E., Massi M., 1984, A&A 136 53
Garmany C. D., 1973, AJ 78, 185
Garrison R. F., 1970, AJ 75, 1001
Gatley I., Becklin E. E., Sellgren K., Werner M. W., 1979, ApJ 233, 575
Gordon M. A., 1987, ApJ 316, 258
Gordon M. A., 1990, ApJ 352, 636
Greene T. P., Young E. T., 1989, ApJ 339, 258 (GY)
Hartigan P., Lada C. J., Stocke J., Tapia S., 1986, AJ 92, 1155
Hildebrand R. H., 1983, QJRAS 24, 267
Hobson M. P., 1992, MNRAS In press
IRAS Explanatory Supplement, 1988, eds. Beichman C.A., et al. NASA-RP-1190, Washington
Kutner M. L., Ulich B. L., 1981, ApJ 250, 341
Mathis J. S., Rumpl W., Nordsieck K. H., 1977, ApJ 217, 425 (MRN)
Mezger P. G., Henderson A. P., 1967, ApJ 147, 471
Miller J. S., 1968, ApJ 151, 473
Panagia N., 1973, AJ 78, 929
Panagia N., Thum C., 1981, A&A 98, 295
Price S. D., Walker R. G., 1976, AFGL report AFGL-TR-76-0208
Rohlfs K., 1986, Tools of Radio Astronomy, Springer-Verlag, Heidelberg
Sargent A. I., 1977, ApJ 218, 736
Sargent A. I., 1979, ApJ 233, 163
Sharpless S., 1959, ApJS 4, 257
Ward-Thompson D., Robson E. I., Whittet D. C. B. Gordon, M. A., Walther D. M., Duncan, W. D., 1989, MNRAS 241, 119
Walker H. J., Cohen M., 1988, AJ 95, 1801
Walker H. J., Cohen M., Volk K., Wainscoat R. J., Schwartz D. E., 1989, AJ 98, 2163
Whittet D. C. B., van Breda I. G., Glass, I. S., 1976, MNRAS 177, 625

This article was processed by the author using Springer-Verlag LaTeX A&A style file 1990.